Lee, Youngsil and Vakil, Gaurang and Watson, Alan James and Wheeler, Patrick (2016) An analytical modeling and estimating losses of power semiconductors in a three-phase dual active bridge converter for MVDC grids. In: IEEE Power and Energy Conference at Illinois, 23-24 Feb 2017, Illinois, USA.

An Analytical Modeling and Estimating Losses of Power Semiconductors in a Three-Phase Dual Active Bridge Converter for MVDC Grids

Youngsil Lee, Gaurang Vakil, Alan. J. Watson, Patrick W. Wheeler
Power Electronics, Machines and Control Research Group
The University of Nottingham
Nottingham, UK
Youngsil.Lee@nottingham.ac.uk

***Abstract*— Due to the increasing installation of renewable and decentralized power sources, Medium-voltage dc (MVDC) grids has been considered for an alternative application to medium-voltage ac (MVAC) application. Three-phase dual active bridge DC-DC (3DAB) converter is proposed as an attractive topology for MVDC grids due to its high power capability, smaller filtering parts, and galvanic isolation. In this paper, a first harmonic approximation (FHA) modeling of 3DAB converter is derived. Using the FHA modeling, a symmetrical modeling of switching devices is introduced and a 4MVA system for 40kV MVDC system has been validated in terms of conduction and switching losses. Experimental implementation of a 10kVA prototype and the results are presented.**

Keywords*— Dual Active Bridge, DC-DC Converter, MVDC, Power losses

I. INTRODUCTION

In the future grid, MVDC grids will be the very flexible technique for collections in renewable energy sources like wind or solar farms and distribution networks within an urban or indusrial areas [1]-[2]. High-power DC-DC converters are one of main technologies to interconnect with MVDC grids. The high-power DC-DC converters must be isolated galvanically from MVDC line to low-voltage dc (LVDC) line for safety operations. Moreover, the galvanic isolation is required for several converter modules of modular topologies operating in series or parallel connection. To meet the requirements of the MVDC applications, the DC-DC converters must be able to deal with bi- or unidirectional power flow. Until now, many DC-DC converter topologies have been presented in different industries such as automotive industry, more electric aircraft (MEA), renewable energy sources, and DC grid collectors. 3DAB Converter which is suitable for high-power application has been studied in [4]-[7] and [9]. Besides, 3DAB converter offers a higher power capability and smaller passive filtering parts compared to single-phase dual active bridge (1DAB) type. One of key parts for the 3DAB converter is a high-power galvanic transformer enabling isolation with MV line for a safety operation and also enabling a soft-switching control which can reduces the switching losses dramatically. The 3DAB converter, depicted in Fig.1, contains two active voltage sourced bridges that are magnetically connected by a medium frequency (MF) transformer. The primary side bridge converts the dc input voltage into a medium-frequency ac voltage that is applied the MF transformer and then the voltage at the secondary terminals of the transformer is rectified by the secondary side bridge. This paper contributes a steady-state modeling methodology of the conducting currents on the power semiconductors and introduces an estimation method of power losses of the devices. In this paper, a 4MVA system for 40kV MVDC grid is validated. This paper presents a 10kVA small scale prototype converter for 1000V supply applications. Finally, experimental validations of the prototype converter are discussed in Section VI.

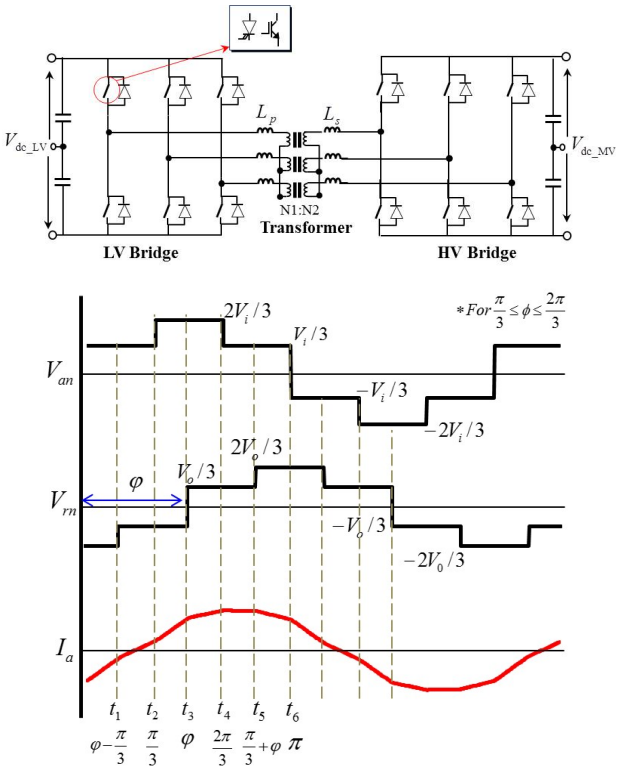

Fig. 1 Characteristic waveforms in the 3DADB converter

978-1-5090-5550-0/17/$31.00 ©2017 IEEE

II. STEADY-STATE MODELING OF 3DAB

Fig. 1 illustrates the resulting typical waveforms in the 3DAB converter for the case of boost application, which the magnitude of V_{rn} is higher than that of V_{an}. A phase shift angle φ is introduced between the voltages applied at the primary and secondary terminals of the transformer. It leads to a voltage drop across the stray inductances, which results in current introduced by a six-step voltage at the transformer is generating. Using the FHA method, RMS values of the primary and secondary winding currents of the transformer can be computed from the following

$$I_{prms} = \frac{V_{in}}{3 \cdot \omega_{sw} \cdot L_\sigma} \cdot \varphi \cdot \sqrt{\frac{2\pi - \varphi}{\pi}} \quad \text{for} \left(0 \le \varphi \le \pi/3\right) \tag{1}$$

$$I_{prms} = \frac{V_{in}}{6 \cdot \omega_{sw} \cdot L_\sigma} \cdot \varphi \cdot \sqrt{\frac{8\pi - 6\varphi}{\pi}} \quad \text{for} \left(\pi/3 \le \varphi \le 2\pi/3\right) \tag{2}$$

Where, $\omega_{sw} = 2\pi \cdot f_{sw}$ is switching frequency and L_σ is the stray inductance of the transformer. The average output power is given by

$$P_o = \frac{V_{in}^2}{\omega_{sw} L_\sigma} \cdot d \cdot \varphi \left[\frac{2}{3} - \frac{\varphi}{2\pi}\right] \quad \text{for} \left(0 \le \varphi \le \pi/3\right) \tag{3}$$

$$P_o = \frac{{V_{in}}^2}{\omega_{sw} L_\sigma} d \left[\varphi - \frac{\varphi^2}{\pi} - \frac{\pi}{18}\right] \quad \text{for} \left(\pi/3 \le \varphi \le 2\pi/3\right) \tag{4}$$

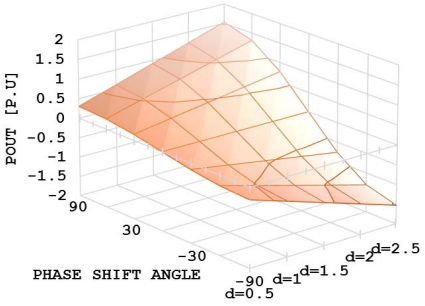

Fig. 2 Output power with different values of φ and d

Calculated output power versus phase shift angle, φ for both forward and reverse power flow is shown in Fig. 2 using d which is dc conversion ratio between primary bridge and secondary bridge as parameter. The per-unit (p.u) results are normalized to the value of base power. During the forward flow, the input side bridge leads the output side bridge, operated as positive phase shifts. In the reverse mode, on the other hand, the output bridge leads the input side bridge. For d =1, it can be seen that full control range under soft-switching is achievable, giving control from zero power for $\varphi = 0$ to maximum power for $\varphi = 90$ and hence, 'd =1' is usually chosen as an optimal design point.

III. MODELING OF SEMICONDUCTOR CONDUCTING CURRENTS

According to Fig. 3, the conducting current of the diode can be expressed by two-step.

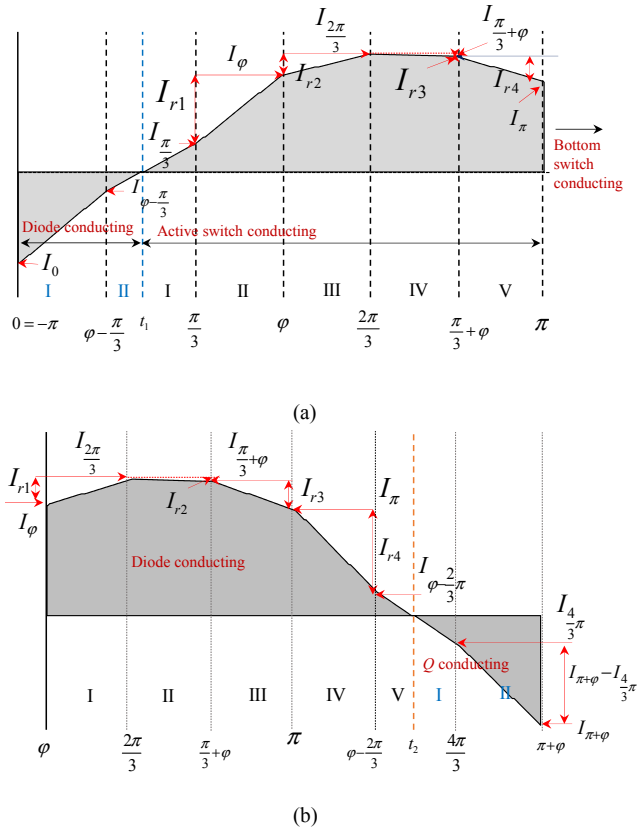

Fig. 3 Conducting currents of (a) the primary side bridge and (b) the secondary side bridge

- For time interval , I

The magnitude of $i(0)$ is calculated as

$$I_0 = I_a(0) = \frac{V_{in}}{3\omega_{sw} L_\sigma}\left[d\pi - 2d\varphi - \frac{2}{3}\pi\right] \tag{5}$$

The magnitude of the current at $\theta = \varphi - \pi/3$ is calculated as

$$I_{\varphi-\frac{\pi}{3}} = I_0 + \frac{V_{in}(1+2d)}{3\omega_{sw} L_\sigma}(\varphi - \frac{\pi}{3}) = \frac{V_{in}}{3\omega_{sw} L_\sigma}\left[d\pi - 2d\varphi - \frac{5}{3}\pi + 3\varphi\right] \tag{6}$$

The total current change during the interval I, where the current is increased from $\theta = 0(-\pi)$ to $\theta = \varphi - \pi/3$, can be written as follows

$$I_{d\_r} = I_0 - I_{\varphi-\frac{\pi}{3}} \tag{7}$$

- For time interval , II

The maximum magnitude of the current can be found at $\theta = \varphi - \pi/3$ and the minimum magnitude is zero hence, the rms value for the time interval can be calculated as

$$I_{rms} = \sqrt{\frac{1}{T}\int_0^{t_1-(\varphi-\frac{\pi}{3})} i^2(\varphi-\frac{\pi}{3})t^2 dt} = \sqrt{\frac{t_1-(\varphi-\frac{\pi}{3})}{T_s}\left[\frac{I^2_{\varphi-\frac{\pi}{3}}}{3}\right]} \tag{8}$$

Where, t_1 is time to the diode conducting current is to zero and semiconductor switch starts to conducting, Assuming half interval between $\pi/3$ and $\varphi - \pi/3$ for the transfer of current from diode to active switch device , total RMS value of the diode conducting current can be calculated by:

$$\begin{aligned} I_{d\_rms\_\text{pri}} &= \sqrt{\frac{1}{T_s}\int_0^{\varphi-\frac{\pi}{3}} I^2(t)dt + \frac{1}{T_s}\int_0^{t_1-(\varphi-\frac{\pi}{3})} I^2(t)dt} \\ &= \sqrt{\frac{\varphi-\frac{\pi}{3}}{T_s}\left[I_0^2 + \frac{I_{d\_r}^2}{3} - I_0 \cdot I_{d\_r}\right] + \frac{t_1-(\varphi-\frac{\pi}{3})}{T_s}\cdot\frac{I^2_{\varphi-\frac{\pi}{3}}}{3}} \end{aligned} \tag{9}$$

On the other hand, the conducting current of the semiconductor switch can be expressed by five-step as shown in Fig. 3. For each time intervals, the rms value can be calculated bellow as

- For time interval , I

The instantaneous current at $\theta = \pi/3$ is represented as follows

$$I_{\frac{\pi}{3}} = \frac{V_{in}}{3\omega_{sw}L_\sigma}\left[\frac{5d}{3}\pi - \pi + 2\varphi - 3d\varphi\right] \tag{10}$$

- For time interval , II

The instantaneous current at $\theta = \varphi$ is represented as follows

$$I_{\varphi} = \frac{V_{in}}{3\omega_{sw}L_\sigma}\left[\frac{4}{3}d\pi - \frac{5}{3}\pi + 4\varphi - 2d\varphi\right] \tag{11}$$

- For time interval , III

$$I_{\frac{2\pi}{3}} = \frac{V_{in}}{3\omega_{sw}L_\sigma}\left[\frac{2}{3}d\pi - \frac{\pi}{3} + 2\varphi - d\varphi\right] \tag{12}$$

- For time interval , IV

$$I_{\frac{\pi}{3}+\varphi} = \frac{V_{in}}{3\omega_{sw}L_\sigma}\left[d\pi - \frac{2}{3}\pi + 3\varphi - 2d\varphi\right] \tag{13}$$

$$I_{Q\_rms\_\text{pri}} = \sqrt{\frac{1}{T_s}\left[\begin{array}{l}\left(\frac{\pi}{3}-t_1\right)\cdot\left(\frac{I^2_{\frac{\pi}{3}}}{3}\right) + \left(\varphi-\frac{\pi}{3}\right)\cdot\left(I_\varphi^2 + \frac{I_{r\_1}^2}{3} - I_\varphi \cdot I_{r\_1}\right) + \left(\frac{2\pi}{3}-\varphi\right)\cdot\left(I^2_{\frac{2\pi}{3}} + \frac{I_{r\_2}^2}{3} - I_{\frac{2\pi}{3}}\cdot I_{r\_2}\right) \\ + \left(\varphi-\frac{\pi}{3}\right)\cdot\left(I^2_{\frac{2\pi}{3}} + \frac{I_{r\_3}^2}{3} - I_{\frac{2\pi}{3}}\cdot I_{r\_3}\right) + \left(\frac{2\pi}{3}-\varphi\right)\cdot\left(I^2_{\frac{\pi}{3}+\varphi} + \frac{I_{r\_4}^2}{3} - I_{\frac{\pi}{3}+\varphi}\cdot I_{r\_4}\right)\end{array}\right]} \tag{15}$$

Where, $I_{r\_1} = I_\varphi - I_{\frac{\pi}{3}}$, $I_{r\_2} = I_{\frac{2\pi}{3}} - I_\varphi$, $I_{r\_3} = I_{\frac{2\pi}{3}} - I_{\frac{\pi}{3}+\varphi}$, and $I_{r\_4} = I_{\frac{\pi}{3}+\varphi} - I_\pi$

$$I_{d\_rms\_\text{sec}} = \sqrt{\frac{1}{T_s}\left[\begin{array}{l}\left(\frac{2\pi}{3}-\varphi\right)\cdot\left(I^2_{\frac{2\pi}{3}} + \frac{I_{r\_1}^2}{3} - I_{\frac{2\pi}{3}}\cdot I_{r\_1}\right) + \left(\varphi-\frac{\pi}{3}\right)\cdot\left(I^2_{\frac{2\pi}{3}} + \frac{I_{r\_2}^2}{3} - I_{\frac{2\pi}{3}}\cdot I_{r\_2}\right) + \left(\frac{2\pi}{3}-\varphi\right)\cdot\left(I^2_{\frac{\pi}{3}+\varphi} + \frac{I_{r\_3}^2}{3} - I_{\frac{\pi}{3}+\varphi}\cdot I_{r\_3}\right) \\ + \left(\varphi-\frac{5\pi}{3}\right)\cdot\left(I_\pi^2 + \frac{I_{r\_4}^2}{3} - I_\pi \cdot I_{r\_4}\right) + \left(\frac{4\pi}{3}-t_2\right)\cdot\left(\frac{I^2_{\varphi-\frac{2\pi}{3}}}{3}\right)\end{array}\right]} \tag{16}$$

Where, $I_{r\_1} = I_{\frac{2}{3}\pi} - I_\varphi$, $I_{r\_2} = I_{\frac{2\pi}{3}} - I_{\frac{\pi}{3}+\varphi}$, $I_{r\_3} = I_{\frac{\pi}{3}+\varphi} - I_\pi$, and $I_{r\_4} = I_\pi - I_{\varphi-\frac{2}{3}\pi}$

$$I_{Q\_rms\_\text{sec}} = \sqrt{\frac{\left(\frac{4\pi}{3}-t_2\right)}{T_s}\cdot\frac{I^2_{\frac{4\pi}{3}}}{3} + \frac{\varphi-\frac{\pi}{3}}{T_s}\left[I^2_{\pi+\varphi} + \frac{\left(I_{\pi+\varphi} - I_{\frac{4}{3}\pi}\right)^2}{3} - I_{\pi+\varphi}\cdot\left(I_{\pi+\varphi} - I_{\frac{4}{3}\pi}\right)\right]} \tag{17}$$

- For time interval , V

$$I_{\pi} = \frac{V_{in}}{3\omega_{sw} L_{\sigma}} \left[-d\pi + 2d\varphi + \frac{2}{3}\pi \right] \tag{14}$$

Therefore, Solving for the rms equation based on the current slope during the intervals, RMS value of the active semiconductor on the primary bridge gives (15). Similarly, the rms currents of secondary side bridge can be calculated. RMS value of diode current is calculated as (16). RMS value of the active semiconductor is calculated as (17).

Since MVDC system applications are considered, insulated gate bipolar transistor (IGBT) and integrated gate commutated thyristor (IGCT) may be the suitable devices for these applications. In general, thyristor-based devices can be suggested for megawatts MV converters due to lower conduction losses compared to IGBT. For the loss calculations and simulations, the characteristics of the IGCT are applied with fast recovery diode. Fig. 4 shows calculated and simulated rms currents of primary side semiconductor devices.

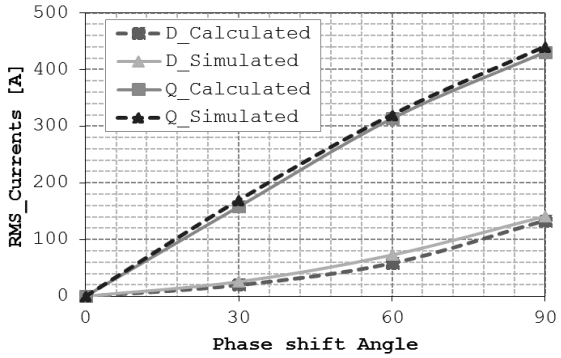

Fig. 4 primary side rms currents versus φ, with *d* as parameter.

IV. LOSSES OF SYMMETRICAL SEMICONDUCTOR

The conduction loss of semiconductor device can be determined by applying the operating condition to the equations derived from the steady-state model of the RMS value of the current. For instance, Fig. 5 shows the variation of conduction losses of the semiconductor devices on primary side bridge as different values of φ. Firstly, diode is conducting negative currents and then active switch is conducting positive currents. The conduction losses are increasing as increasing the phase shift angle, which results in an increase in instantaneous inductance current.

Calculated and simulated conduction losses versus currents are shown in Fig. 6. Comparing the diagram, one can conclude that the differences between simulated and calculated losses are likely due to the effect of resistive load on the converter, winding resistance, etc.

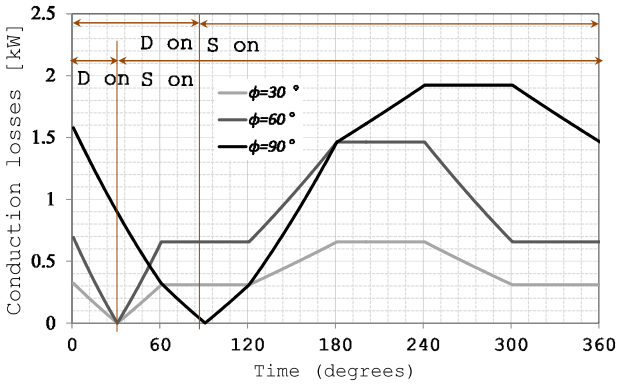

Fig. 5 Instantaneous conduction losses of primary side bridge for steady-state condition

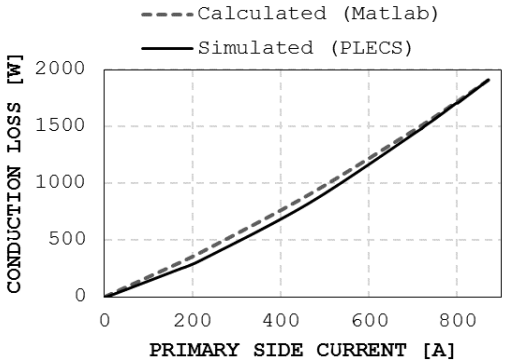

Fig.6 Comparison of calculated and simulated power losses of primary side IGCTs

Average conduction losses can be calculated by

$$P_{avg\_con\_igct}(t) = \frac{1}{T_{sw}} \int_0^{T_{sw}} (v_{T0} \cdot i_c(t) + r_0 \cdot i_c^2(t))dt \tag{18}$$
$$= v_{T0} \cdot I_{avg\_igct} + r_0 \cdot I_{rms\_igct}^2$$

$$P_{avg\_con\_diode}(t) = \frac{1}{T_{sw}} \int_0^{T_{sw}} (v_{D0} \cdot i_D(t) + r_0 \cdot i_D^2(t))dt \tag{19}$$
$$= v_{D0} \cdot I_{avg\_diode} + r_0 \cdot I_{rms\_diode}^2$$

Where, r_0 is the slope resistances of the IGCT/IGBT and diode, v_{T0} and v_{D0} are the threshold voltages of the IGCT/IGBT and diode respectively. During the switching process of the converter, a significant of the stored energy in the switch capacitance may be transferred from the switches to another hence, the switching losses amount to a significant part of the total losses. In steady-state operation, each switches of the 3DAB converter are turned-on and turned-off during one half-cycle respectively. If the 3DAB

converter operates in zero voltage switching (ZVS) range, turn-on losses of the semiconductors can be eliminated. Therefore, in the ZVS operation, only conduction and turn-off switching losses can be expected to contribute the main factor of semiconductor losses. Furthermore, in the future step, an analysis of switching loss in each hard-switching and soft-switching range will be required in order to accurately determine the power dissipated in the semi-conductor. In this work, a simple calculation is applied to estimate the switching losses during the ZVS operation. Turn-off loss is calculated from the turn-off energy loss curve given in the datasheet for the corresponding turn-off current and voltage. Hence the total switching losses are calculated by summing the losses of the individual switching events

$$P_{sw\_off} = \frac{1}{t_{off}} \sum E_{OFF} \tag{20}$$

Similarly, the calculation of the turn-on loss corresponds to the turn-off loss

$$P_{sw\_on} = \frac{1}{t_{on}} \sum E_{ON} \tag{21}$$

Finally, average switching losses of IGBT/IGCTs and Diodes are calculated from

$$P_{sw\_LV} = n\left[(E_{OFF\_igct} + E_{OFF\_diode}) \times f_{sw} \times \frac{V_{CE}}{V_{CC}} \right] \tag{22}$$

$$P_{sw\_HV} = n\left[(E_{OFF\_igct} + E_{OFF\_diode}) \times f_{sw} \times \frac{V_{CE}}{V_{CC}} \right] \tag{23}$$

Where, n is the number of devices, f_{sw} is the switching frequency, V_{CE} is the operating voltage, and V_{CC} is the maximum voltage defined from the energy loss curves.

V. SIMULATION VALIDATION

To validate the loss estimation, a 3DAB converter based on the steady-state model has been designed to be transferring 4MVA power. The model is operating with a switching frequency 1000Hz. Using (3) and (4), the allowed value of the stray inductance that ensures soft switching of the 3DAB converter can be calculated. In this case, the calculated straystary inductance L_σ is 0.636mH. By the simulation, the power losses of the two semiconductor devices (IGBT and IGCT) are compared in the 3DAB converter model. The software PLECS has been used as simulation tool. In this simulation, the 3DAB converter model is connected to ideal DC source in order to implicate the evaluation. Since the devices are rated with 2.8kV blocking dc voltage, two devices per converter arm on the primary side are connected in series and hence total 12 IGCT/IGBTs and 12 diodes are applied in the primary bridge. In the contrary, the secondary side connected to 40 kV can be realized with 18 devices in series. Total 108 IGCTs or IGBTs and diodes are used to energize the peak power demand.

TABLE I. Simulation parameters

Primary side voltage [kV]	4
Secondary side voltage [kV]	40
Rated Power [MVA]	4
DC conversion ratio '*d*'	1
Switching frequency [kHz]	1
Turns ratio	1:10
IGCT	ABB 5SHY 50L5500 [8]
StakPak IGBT Module	ABB 5SNA 2000K451300 [8]
Diode	ABB 5SDF20L4520 [8]
Semiconductor blocking DC Voltage [kV]	2.8

Fig. 6 shows the conduction losses of the IGCTs and IGBTs on the primary bridge (4kV) and secondary bridge (40kV) sides. Ftorm the comparison, application of the IGCTs on primary bridge shows a slightly lower loss for $\varphi \geq \pi/3$ compared to the IGBTs. However, the IGBT devices show a better performance if $\varphi \leq \pi/6$. The conduction losses of the IGCTs on secondary side are higher than the IGBTs at all points. This is mainly due to the higher threshold value of the IGCT device compared to the collecter-emitter voltage of the IGBT module corresponding to zero current.

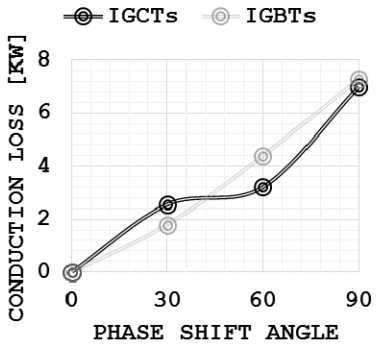

(a)

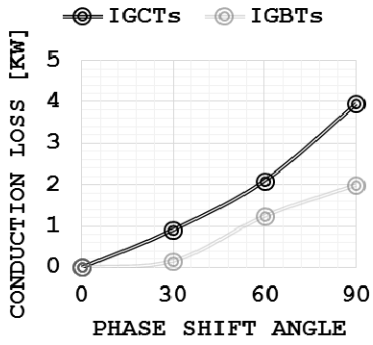

(b)

Fig. 6 Comparison of conduction loss of IGCT & IGBT device: (a) on primary (4kV) bridge (b) on secondary (40kV) bridge

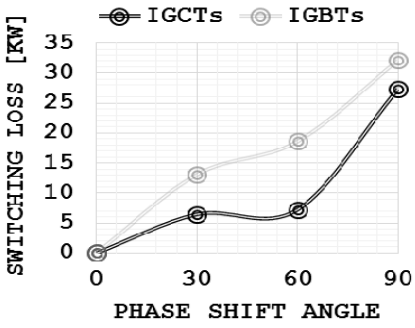

(a)

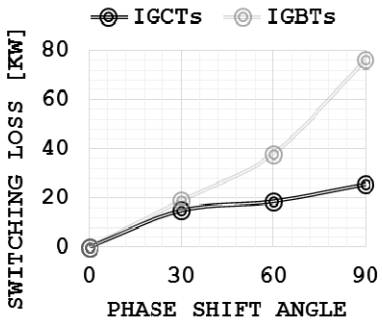

(b)

Fig. 7 Comparison of switching loss of IGCT & IGBT device : (a) on primary(4kV) bridge, (b) on secondary (40kV) bridge

The switching losses of IGCTs and IGBTs are more significant issue to efficiency of the 3DAB converter. From Fig. 7, it can be found that the turning-off losses of the IGBTs are higher than the IGCTs at all points. At $\varphi = \pi/2$, the switching losses of the IGBTs of primary bridge is found to be 32.13kW, which is little higher than the IGCTs. However, the switching losses of them are very higher than IGCTs as shown in Fig. 7(b). It seems to that the IGCTs show a better performance for turning-off switching.

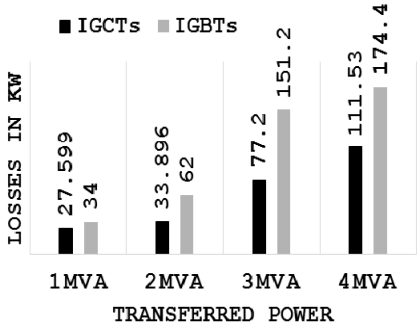

(a)

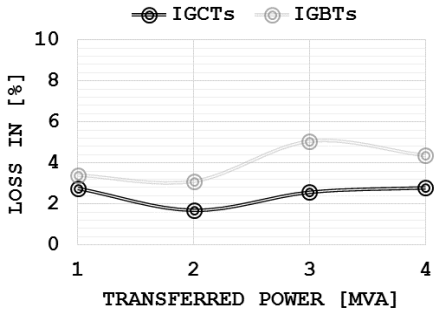

(b)

Fig. 8 Semi-conductor losses in the 3DAB converter in relation to the transferred power

The breakdown of an amount of conduction and switching losses in Fig. 8 shows increasing both devices with phase shift angle increase. At $\varphi = \pi/2$ (0.61 p.u rated power), the total losses of the IGBTs are found to be 117.5 kW, which is 54.5 % higher than the losses occurring in the IGCTs of the 3DAB converter. At all transferred power, the losse of the IGBTs are high when compared to the IGCTs as highlighted in Fig. 8(a). This is mainly because of an increase in the IGBT turn-off switching losses on the primary bridge and secondary bridge. Fig. 8 (b) shows the relative losses in relation to the transferred power. From the plot, the 3DAB converter shows a better performance if the transferred power is about 0.5 p.u. At rated power, the efficiency is about 97.2 % if IGCTs are applied compared with an efficiency of 95.7% of IGBTs. With a value of 0.75 p.u at rated power, the efficiency of the 3DAB becomes lower. In this condition, the 3DAB operates at d=1 to remain the soft-switching operation. At the maximum power transfer operation point, $\varphi = \pi/2$, dc conversion ratio will be increased to increase the transferred power. However, the 3DAB converter has poor efficiency due to the high voltage

transformation ratio. Thus, using the IGCT, the efficiency of the 3DAB converter is increased by roughly 1.6 % at rated power, 2.5 % at 0.75 pu power, and 0.6 % at half rated power respectively compared to the converter using IGBTs.

VI. 10KVA SMALL SCALE PROTOTYPE CONVERTER

For the practical implementation, a 10kVA small scale prototype converter has been built up. The prototype uses "SKM75GB176D" Trench IGBT modules from SEMIKRON [10] and is operating at a switching frequency of 1kHz. The input dc-link voltage is set to 500V. The three-phase transformer is manufactured using the design strategy introduced in [6]. The symmetric stray inductance was measured around $L_\sigma = 92uH$. Turn radio of the transformer is 1:2 hence, the output dc-link voltage is set to 1000V. In the experiment, the control phase shift angle is set to $\varphi = 3.0°$ due to the low value of the stray inductance.

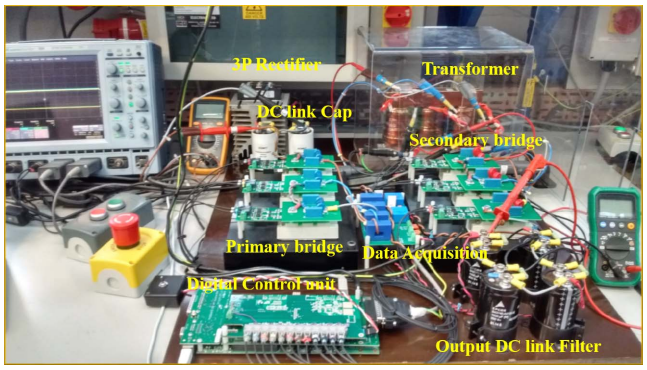

Fig. 9 A 10kVA small scale prototype converter

Fig. 9 and 10 show the prototype and measurement results. Fig. 10 (a) shows the square waves of the transformer winding produced by the two bridges. A small phase shift can be seen between the primary and secondary winding waves and it is equal as the control phase shift angle. Fig. 10 (b) shows the switched current waves of the two windings. In the case of the small control phase shift angle, the switched harmonics of the transformer currents are generated clearly by the six-step time intervals. The DC link currents on each side of the 3DAB converter when it is implemented under the open control scheme is shown in Fig. 10 (c). Fig. 11 shows the loss distribution among the semiconductor devices for the primary bridge and the secondary bridge respectively. Comparing the HV secondary bridge, one generally finds the losses in the IGBT modules in the LV primary bridge switches are drastically increased toward higher power level (over 50 % full level). It is due to the fact that conduction losses are increased with the increases in the transferred power. On the other side, the switching losses with HV level are slightly higher than the LV bridge switches. The measured efficiencies are presented against transferred power in Fig. 12. As can be seen, the efficiency of the 3DAB converter increases generally toward higher powers. Here a 99.13% efficiency of the IGBT modules is reached at the rated power. It can be seen that efficiencies above 99% can be achieved down to 20 % of the rated power level. This is mainly due to the lower turn-on and turn-off energy losses of the IGBT module in relation to the 3DAB converter. Note that the transformer with peak efficiency of almost 97% at rated power has been applied into the converter. Hence, from the measured results, it can be seen that the transformer losses clearly dominate overall converter losses. It has further been illustrated that using a high efficiency transformer can potentially increase the overall performance of the 3DAB converter.

VII. CONCLUSION

This paper has presented a steady-state model for a symmetrical 3DAB converter. Expressions for the rms values of switch currents, along with peak and rms currents of the stray inductance of the transformer were obtained from the model. These mathematical models are useful in predicting power losses and enable a study of the converter characteristics. The steady-state operation of the 3DAB converter has been verified through simulations and also validated losses of power-electronics such as IGBT and IGCT. The simulation results confirm that IGCT devices can be selected as an optimal power-electronics switch for high power conversion systems. The implementation was proved effective during the validation of the prototype converter on a 1000V supply system at powers upto 10kVA. The results indicate that the main switching devices with recorded maximum efficiency of 99.73 % may be proposed as an efficient component in the converter topology.

REFERENCES

[1] A. Korompili, A. Sadu, F. Ponci and A. Monti, "Flexible Electric Networks of the Future: Project on Control and Automation in MVDC grids," *International ETG Congress 2015; Die Energiewende - Blueprints for the new energy age; Proceedings of,* Bonn, Germany, 2015, pp. 1-8.

[2] M. Stieneker and R. W. De Doncker, "Medium-voltage DC distribution grids in urban areas," *2016 IEEE 7th International Symposium on Power Electronics for Distributed Generation Systems (PEDG)*, Vancouver, BC, 2016, pp. 1-7.

[3] A. J. Watson, P. W. Wheeler and J. C. Clare, "Field programmable gate array based control of Dual Active Bridge DC/DC Converter for the UNIFLEX-PM project," *Power Electronics and Applications (EPE 2011), Proceedings of the 2011-14th European Conference on*, Birmingham, 2011, pp. 1-9.

[4] R. L. Steigerwald, R. W. De Doncker and H. Kheraluwala, "A comparison of high-power DC-DC soft-switched converter topologies," in *IEEE Transactions on Industry Applications*, vol. 32, no. 5, pp. 1139-1145, Sep/Oct 1996.

[5] M. N. Kheraluwala, R. W. Gascoigne, D. M. Divan and E. D. Baumann, "Performance characterization of a high-power dual active bridge DC-to-DC converter," in *IEEE Transactions on Industry Applications*, vol. 28, no. 6, pp. 1294-1301, Nov/Dec 1992.

[6] Y. Lee, G. Vakil, R. Feldman, A. Goodman and P. Wheeler, "Design optimization of a high-power transformer for three-phase dual active

bridge DC-DC converter for MVDC grids," *8th IET International Conference on Power Electronics, Machines and Drives (PEMD 2016)*, Glasgow, 2016, pp. 1-6.
[7] R. W. De Doncker, D. M. Divan and M. H. Kheraluwala, "A three-phase soft-switched high power density DC/DC converter for high power applications," *Industry Applications Society Annual Meeting, 1988., Conference Record of the 1988 IEEE*, Pittsburgh, PA, USA, 1988, pp. 796-805, vol. 1.
[8] [Online]. Available: http://new.abb.com/semi-conductors
[9] Y. Lee, G. Vakil, R. Feldman, A. J. Watson and P. W. Wheeler, "A high-power DC-DC converter based dual active bridge for MVDC grids on offshore wind farms," *2016 18th European Conference on Power Electronics and Applications (EPE'16 ECCE Europe)*, Karlsruhe, 2016, pp. 1-10.
[10] [Online]. Available: https://www.semikron.com/products/product-classes/igbt-modules/detail/skm75gb176d-22890850.html

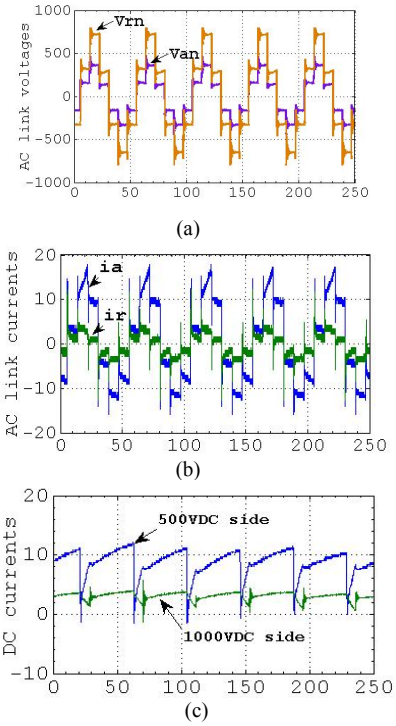

Fig. 10 Measurement results of the 10kVA prototype converter: (a) phase voltages, (b) currents of the Y-connected transformer, and (c) dc currents

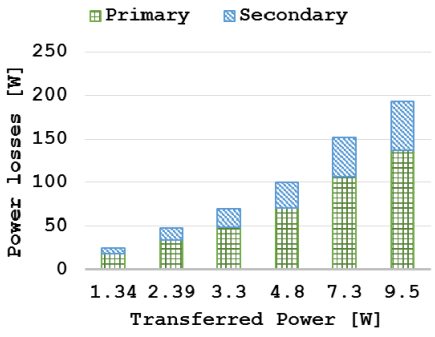

Fig. 11 Losses of IGBT modules varied with transferred power

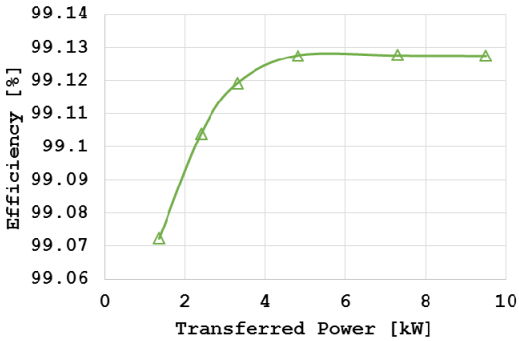

Fig. 12 Efficiency varied with transferred power